

Multiscale finite element method for Stokes-Darcy model

Yachen Hong*, Wenhan Zhang[†], Lina Zhao[‡], Haibiao Zheng[§]

January 9, 2024

Abstract

This paper explores the application of the multiscale finite element method (MsFEM) to address steady-state Stokes-Darcy problems with BJS interface conditions in highly heterogeneous porous media. We assume the existence of multiscale features in the Darcy region and propose an algorithm for the multiscale Stokes-Darcy model. During the offline phase, we employ MsFEM to construct permeability-dependent offline bases for efficient coarse-grid simulation, with this process conducted in parallel to enhance its efficiency. In the online phase, we use the Robin-Robin algorithm to derive the model's solution. Subsequently, we conduct error analysis based on L^2 and H^1 norms, assuming certain periodic coefficients in the Darcy region. To validate our approach, we present extensive numerical tests on highly heterogeneous media, illustrating the results of the error analysis.

Keywords: MsFEM; multiscale; steady Stokes-Darcy flow; highly heterogeneous; Robin-Robin algorithm.

1 Introduction

In this paper, we design and analyze an efficient numerical method based on the multiscale finite element method (MsFEM) framework for Stokes-Darcy system. The Stokes-Darcy problem has gained significant attention over the last decade, particularly following the influential works by Discacciati et al. [9] and Layton et al [18]. Such models can be used to describe physiological phenomena like hydrological systems in which surface water percolates through rocks and sand, and various industrial processes involving filtration, reservoir simulation, nuclear water storage and underground water contamination. In these fields, it is often encountered with situations involving multiple scales; for example complex rock matrices when modelling sub-surface flows or random placements of buildings, people and trees in the context of urban canopy flows. Hence, it is necessary to take into consideration the presence of multiple scales in the Stokes-Darcy model.

These multiscale Stokes-Darcy problems can arise from either the presence of highly oscillatory coefficients within the system or the heterogeneity of the domain; These problems can be very challenging due to the necessary resolution for achieving meaningful results. Constrained by computational cost and prohibitive size, numerous practical problems remain beyond reach through direct simulations. On the other hand, there is currently no effective algorithm for the multiscale problem of Stokes-Darcy with BJS (Beavers-Joseph-Saffman) interface conditions. Thus, it is desirable to develop an efficient computational algorithm to solve multiscale problems without being confined to solving fine scale solutions and establish the corresponding error analysis.

*Department of Mathematics, East China Normal University, Shanghai.

[†]Department of Mathematics, East China Normal University, Shanghai.

[‡]Department of Mathematics, City University of Hong Kong, Kowloon Tong, Hong Kong SAR.

[§]Department of Mathematics, Key Laboratory of MEA (Ministry of Education) and Shanghai Key Laboratory of PMMP, East China Normal University, Shanghai.

Prior to presenting our multiscale Stokes-Darcy multiscale techniques and their application to the Stokes-Darcy problem. In addition to some traditional upscaling techniques, nowadays, various multi-scale methods can be employed to solve multi-scale problems. One type of multiscale method involves generating new basis functions, where the aim is to solve the problem on a coarse grid using carefully designed multiscale basis functions. Notable multiscale methods such as multiscale finite method (MsFEM) by Hou and Wu [14, 7]. MsFEM's applicability broadens to situations where analytical representations of microscopic elements are unavailable, given that the multiscale basis is calculated rather than modeled. Within the last decades, several methods sprung from similar purpose namely, the generalized multiscale finite element method (GMsFEM) [11, 8], the multiscale finite volume method (MsFVM) [13, 17, 10], the heterogeneous multiscale method (HMM) [20], the variational multiscale method (VMS) [16], the multi-scale mortar mixed finite element method (MMMFEM) [4], the localized orthogonal method (LOD) [19], the multiscale hybrid-mixed method (MHM) [3]. Multiscale methods have demonstrated their ability to handle the complexity associated with industry-standard grid representation and flow physics.

Several theoretical and numerical studies have been done in the couple years to solve Stokes-Darcy problem. Jun Yao et al. [24] presented a multiscale mixed finite element method (MsMFEM) for fluid flow in fractured vuggy media. ABDULLE et al. [1] introduced Darcy-Stokes finite element heterogeneous multiscale method (DS-FE-HMM) in porous media. Girault et al. [12] investigated mortar multiscale numerical methods for coupled Stokes and Darcy flows with the Beavers-Joseph-Saffman(BJS) interface condition. Ilona Ambartsumyan et al.[2] introduced stochastic multiscale flux basis for Stokes-Darcy flows. To date, although there are many multiscale methods available for addressing the Stokes-Darcy problem, MsFEM has not been applied to the Stokes-Darcy problem with BJS interface conditions and conducted theoretical error analysis.

In this paper we propose an Msfem method to solve steady Stokes-Darcy problem with BJS interface condition and derive a fully a priori error analysis. Our objective is to propose effective methods that minimize computational efforts when dealing with multiscale phenomena in the Darcy region. While the basis functions of MsFEM have seen widespread use, their application in the context of steady-state Stokes-Darcy problems with BJS interface conditions is notably lacking, let alone the presence of comprehensive error analysis. We use multiscale finite methods in the Darcy region, assuming the presence of multiscale phenomena, and apply standard finite element methods in the Stokes region, with the coupling between the two regions established through an interface. The multiscale finite element basis functions are inspired by Hou's work [14, 7] and generated using parallel methods. In the Stokes region, we employ standard MINI elements for the basis functions. Additionally, we utilize the Robin-Robin algorithm to obtain the final solution. Then, we conducted error analysis in terms of L^2 and H^1 , assuming the Darcy region possesses certain periodic coefficients. Finally, numerical examples will validate the effectiveness of our algorithm and error analysis.

The rest of the paper is organized as follows. In section 2, we introduce the Stokes-Darcy model. Next, we introduced the finite element space and the multiscale basis function space. Meanwhile, we also introduced some homogenization principles and certain model results. The Multiscale finite Stokes-Darcy algorithm are presented in Section 3. It is mainly divided into two parts: offline and online phase. The corresponding H^1 and L^2 error estimates is shown in Section 4. Numerical experiments are presented in Section 5.

2 Preliminaries.

2.1 Stokes-Darcy model with BJS interface condtion

Let us consider the following mixed model for coupling a fluid flow and a porous media flow in a bounded domain $\Omega \subset \mathbf{R}^d, d = 2, 3$. Here $\Omega = \Omega_f \cup \Gamma \cup \Omega_p$, where Ω_f and Ω_p are two disjoint, connected and bounded domains occupied by fluid flow and porous media flow and $\Gamma = \bar{\Omega}_f \cap \bar{\Omega}_p$ is the interface. For simplicity, we assume $\partial\Omega_p$ and $\partial\Omega_f$ are smooth enough in the rest of this paper. We denote $\Gamma_f = \partial\Omega_f \cap \partial\Omega$, $\Gamma_p = \partial\Omega_p \cap \partial\Omega$ and we also denote by \mathbf{n}_p and \mathbf{n}_f the unit outward normal vectors on $\partial\Omega_p$ and $\partial\Omega_f$, respectively. See Fig. 1 for a sketch.

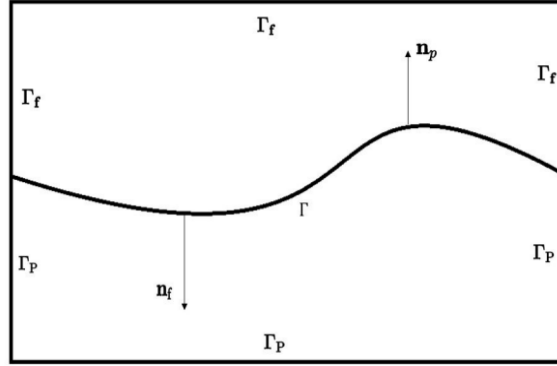


Figure 1:
A global domain Ω consisting of a fluid flow region Ω_f
and a porous media flow region Ω_p separated by an interface Γ .

The fluid motion in the fluid region Ω_f is governed by the Stokes equations

$$\begin{cases} -\nabla \cdot (\mathbb{T}(\mathbf{u}_f, p_f)) = \mathbf{g}_f, & \text{in } \Omega_f, \\ \nabla \cdot \mathbf{u}_f = 0, & \text{in } \Omega_f, \end{cases} \quad (2.1)$$

where

$$\mathbb{T}(\mathbf{u}_f, p_f) = -p_f \mathbb{I} + 2v \mathbb{D}(\mathbf{u}_f), \quad \mathbb{D}(\mathbf{u}_f) = \frac{1}{2} (\nabla \mathbf{u}_f + \nabla^T \mathbf{u}_f),$$

are the stress tensor and the deformation rate tensor, $v > 0$ is the kinetic viscosity and \mathbf{g}_f is the external force.

We assume that the porous region possesses multiple scales. The fluid motion in the porous medium region Ω_p is governed by

$$\begin{cases} \nabla \cdot \mathbf{u}_d = g_p, & \text{in } \Omega_p, \\ \mathbf{u}_d = -\mathbb{K}_\epsilon \nabla \phi_p, & \text{in } \Omega_p, \end{cases} \quad (2.2)$$

where \mathbb{K}_ϵ denotes the hydraulic conductivity in Ω_p , which is a positive symmetric tensor and includes multiscale information where ϵ is a small parameter and g_p is a source term. The first equation is the saturated flow model and the second equation is the Darcy's law. Here $\phi_p = z + \frac{p_p}{\rho g}$ is the piezometric (hydraulic) head, where p_p represents the dynamic pressure, z the height from a reference level, ρ the density and g the gravitational constant, and \mathbf{u}_d is the flow velocity in the porous medium which is proportional to the gradient of ϕ_p , namely, the Darcy's law.

Combining the two equations in (2.2), we get the equation for the piezometric head, which we will refer to simply as the Darcy equation:

$$-\nabla \cdot (\mathbb{K}_\epsilon \nabla \phi_p) = g_p, \quad \text{in } \Omega_p. \quad (2.3)$$

Eqs. (2.1) and (2.3) are completed and coupled together by the following boundary conditions:

$$\mathbf{u}_f = 0 \quad \text{on } \Gamma_f, \quad \phi_p = 0 \quad \text{on } \Gamma_p,$$

and the interface conditions on Γ :

$$\mathbf{u}_f \cdot \mathbf{n}_f = \mathbf{u}_p \cdot \mathbf{n}_p = -\mathbb{K}_\epsilon \nabla \phi_p \cdot \mathbf{n}_p, \quad (2.4)$$

$$-\mathbf{n} \cdot \mathbb{T}(\mathbf{u}_f, p_f) \cdot \mathbf{n} = g(\phi_p - z), \quad (2.5)$$

$$-\boldsymbol{\tau}_i \cdot \mathbb{T}(\mathbf{u}_f, p_f) \cdot \mathbf{n}_f = \frac{\alpha \nu \sqrt{d}}{\sqrt{\text{trace}(\Pi)}} \mathbf{u}_f \cdot \boldsymbol{\tau}_i. \quad (2.6)$$

where $\boldsymbol{\tau}_i, i = 1, \dots, d-1$ is an orthonormal basis of the tangential space on Γ and g the gravitational acceleration and we assumed that $g = 1$ in the following. α is an experimentally determined parameter and Π represents the permeability, which has the following relation with the hydraulic conductivity, $\mathbb{K}_\epsilon = \frac{\Pi g}{v}$. The first interface condition (2.4) describes the mass conservation and the second equation (2.5) represents the balance of momentum. The third interface condition (2.6) is called Beavers-Joseph-Saffman condition, which means the tangential components of the normal stress force is proportional to the tangential components of the fluid velocity[5].

Furthermore, we assume \mathbb{K}_ϵ is symmetric, periodic, and uniformly elliptic. There exist two constants $\lambda_{\max} > 0, \lambda_{\min} > 0$ such that

$$0 < \lambda_{\min} |\mathbf{x}|^2 \leq \mathbb{K}_\epsilon \mathbf{x} \cdot \mathbf{x} \leq \lambda_{\max} |\mathbf{x}|^2, \quad \forall \mathbf{x} \in \Omega_p$$

Also, we assume

$$\mathbf{g}_f \in \mathbf{L}^2(\Omega_f), \quad g_p \in L^2(\Omega_p), \quad \mathbb{K}_\epsilon \in L^\infty(\Omega_p)^{d \times d}.$$

For simplicity, we consider 2D problems through the full text. We reserve Ω for a domain (bounded and open set) with Lipschitz boundary and d for spacial dimension ($d = 2$). The Einstein summation convention is adopted, means summing repeated indexes from 1 to d . The Sobolev spaces $W^{k,p}$ and H^k are defined as usual (see e.g., [6]) and we abbreviate the norm Sobolev space $H^k(D)$ as $\|\cdot\|_{k,D}$.

Later on we need to introduce some Hilbert spaces

$$\begin{aligned} \mathbf{V}_f &= \{ \mathbf{v}_f \in \mathbf{H}^1(\Omega_f) : \mathbf{v}_f|_{\Gamma_{f,D}} = 0 \}, \\ X_p &= \{ \psi \in H^1(\Omega_p) : \psi|_{\Gamma_{p,D}} = 0 \}, \\ Q_f &= L_0^2(\Omega_f) = \left\{ q_f \in L^2(\Omega_f) : \int_{\Omega_f} q_f = 0 \right\}. \end{aligned} \quad (2.7)$$

The space $L^2(D)$, where $D = \Omega_f$ or Ω_p , is equipped with the usual L^2 -scalar product (\cdot, \cdot) and L^2 -norm $\|\cdot\|_{L^2(D)}$. The spaces H_f and H_p are equipped with the following norms:

$$\begin{aligned} \|\nabla u\|_{L^2(\Omega_f)} &= \sqrt{(\nabla u, \nabla u)_{\Omega_f}} \quad \forall u \in \mathbf{V}_f, \\ \|\nabla \phi\|_{L^2(\Omega_p)} &= \sqrt{(\nabla \phi, \nabla \phi)_{\Omega_p}} \quad \forall \phi \in X_p. \end{aligned}$$

Let us denote

$$U = \mathbf{V}_f \times X_p.$$

Hence, we use the notational convention that $\mathbf{u} = (\mathbf{u}_f, \phi_p)$ and $\mathbf{v} = (\mathbf{v}_f, \psi_p)$. They all belong to \mathbf{U} : for $\mathbf{g}_f \in \mathbf{L}^2(\Omega_f)$ and $g_p \in L^2(\Omega_p)$, find $(\mathbf{u}, p_f) \in \mathbf{U} \times Q_f$ such that $\forall (\mathbf{v}, q_f) \in \mathbf{U} \times Q_f$ and \mathbf{U}' is the dual space of \mathbf{U} , $P_\tau(\cdot)$ is the projection onto the local tangential plane that can be explicitly expressed as $P_\tau(\mathbf{v}_f) = \mathbf{v}_f - (\mathbf{v}_f \cdot \mathbf{n}_f) \mathbf{n}_f$

$$a(\mathbf{u}, \mathbf{v}) - (p_f, \nabla \cdot \mathbf{v}_f)_{\Omega_f} + (q_f, \nabla \cdot \mathbf{u}_f)_{\Omega_f} = (\mathbf{F}, \mathbf{v})_{\mathbf{U}'}, \quad (2.8)$$

where

$$\begin{aligned} a(\mathbf{u}, \mathbf{v}) &= 2\nu (\mathbb{D}(\mathbf{u}_f), \mathbb{D}(\mathbf{v}_f))_{\Omega_f} + g(\phi_p, \mathbf{v}_f \cdot \mathbf{n}_f)_\Gamma \\ &\quad + \left(\frac{\alpha v \sqrt{d}}{\sqrt{\text{trace}(\Pi)}} P_\tau(\mathbf{u}_f), \mathbf{v}_f \right)_\Gamma \\ &\quad + g(\mathbb{K}_\epsilon \nabla \phi_p, \nabla \psi_p)_{\Omega_p} - g(\psi_p, \mathbf{u}_f \cdot \mathbf{n}_f)_\Gamma, \\ (\mathbf{F}, \mathbf{v})_{\mathbf{U}'} &= (\mathbf{g}_f, \mathbf{v}_f)_{\Omega_f} + g(g_p, \psi_p)_{\Omega_p} + g(z, \mathbf{v}_f \cdot \mathbf{n}_f)_\Gamma. \end{aligned} \quad (2.9)$$

We know that there exists a positive constant $\beta > 0$ such that the following Ladyzhenskaya-Babuška-Brezzi (LBB) condition holds:

$$\inf_{q_f \in Q_f} \sup_{\mathbf{v}_f \in \mathbf{X}_f} \frac{(q_f, \nabla \cdot \mathbf{v}_f)_{\Omega_f}}{\|q_f\|_{Q_f} \|\mathbf{v}_f\|_{\mathbf{X}_f}} \geq \beta.$$

Theorem 2.1 (Proofs in [21]). *The weak formulation (2.8) of Stokes-Darcy problem is well-posed.*

Remark 2.1. *For the purpose of later analysis, we recall some inequalities: $\forall v \in H^1(D)$*

$$\begin{aligned}\|v\|_{L^2(\partial D)} &\leq c_0 \|v\|_{L^2(D)}^{\frac{1}{2}} \|v\|_{H^1(D)}^{\frac{1}{2}}, \\ \|v\|_{L^2(\partial D)} &\leq c_1 \|v\|_{H^1(D)}, \\ \|\nabla v\|_{L^2(D)} &\leq c_2 \|D(v)\|_{L^2(D)}.\end{aligned}$$

2.2 Finite element approximation

We give the finite element approximation of this model. For any given small parameter $h > 0$, we construct the regular triangulations $\mathcal{T}_h, \mathcal{T}_{fh}$ and \mathcal{T}_{ph} of Ω, Ω_f and Ω_p .

Let $\mathbf{V}_{fh} \subset \mathbf{V}_f, X_{ph} \subset X_p$, and $Q_{fh} \subset Q_f$ be finite element spaces such that the space pair $(\mathbf{V}_{fh}, Q_{fh})$ satisfies the discrete LBB condition : there exists a constant $\beta > 0$, independent of mesh, such that

$$\inf_{0 \neq q_h \in Q_{fh}} \sup_{0 \neq \mathbf{v}_h \in \mathbf{X}_{fh}} \frac{(q_h, \nabla \cdot \mathbf{v}_h)_{\Omega_f}}{\|\mathbf{v}_h\|_1 \|q_h\|_0} > \beta. \quad (2.10)$$

Here we choose MINI finite element pair for $(\mathbf{V}_{fh}, Q_{fh})$ and multiscale finite element for V_{ph} . Define

$$U_h = \mathbf{V}_{fh} \times X_{ph}.$$

We define Lagrange element space $\mathcal{P} := \{u \in C(\bar{\Omega}), \forall T \in \mathcal{T}_h, u|_T \in \mathcal{P}_1(T)\}$ and consider a triangulation \mathcal{T}_{ph} and base functions $(\psi^i)_{1 \leq i \leq Nb_{\text{vertex}}} \in \mathcal{P}$ which consists of the globally continuous on \mathcal{T}_{ph} and affine on each triangle $K \subset \mathcal{T}_{ph}$ functions which satisfy: $\psi^i(x_j) = \delta_{ij}$, where $(x_j)_{1 \leq j \leq Nb_{\text{vertex}}}$ are the vertices of the coarse mesh (Nb_{vertex} the set of interior vertices of the coarse mesh) and δ_{ij} is the Kronecker symbol. The multiscale finite element basis functions $(\eta_i^{MsFEM})_{1 \leq i \leq Nb_{\text{vertex}}}$ which take into account the multiscale of the coefficients. More precisely we compute $\eta_{i,K}^{MsFEM}$, such that for any triangle $K \subset \mathcal{T}_{ph}$,

$$\begin{cases} -\operatorname{div}(\mathbb{K}_\epsilon(\frac{x}{\epsilon}) \nabla \eta_{i,K}^{MsFEM}) = 0 & \text{in } K, \\ \eta_{i,K}^{MsFEM} = \psi^i & \text{on } \partial K. \end{cases}$$

In practice, we do not have access to $\eta_{i,K}^{MsFEM}$. We build $\eta_{i,K}^{MsFEM, h_{finer}}$, an approximation of $\eta_{i,K}^{MsFEM}$ on a finer embedded grid of mesh size h_{finer} , with \mathcal{P}_1 FE. See Fig. 2.

Therefore, we can get the multiscale finite element basis function $\{\eta_i^{MsFEM} = \cup_{K \in \mathcal{K}^h} \eta_{i,K}^{MsFEM}\}$ and a simple observation tells that η_i^{MsFEM} is locally support.

Then we can introduce

$$X_{ph} = \operatorname{span} \{\eta_i^{MsFEM} : i = 1, \dots, Nb_{\text{vertex}} ; K \in \mathcal{K}^h\}.$$

Therefore, the coupled finite element Galerkin approximation of reads:

Coupled Finite Element Scheme: find $\underline{\mathbf{u}}_h = (\mathbf{u}_{fh}, \phi_{ph}) \in \mathbf{U}_h, p_{fh} \in Q_{fh}$ such that for any $\underline{\mathbf{v}}_h = (\mathbf{v}_{fh}, \phi_{ph}) \in \mathbf{U}_h$ and $q_{fh} \in Q_{fh}$

$$a(\underline{\mathbf{u}}_h, \underline{\mathbf{v}}_h) - (p_{fh}, \nabla \cdot \mathbf{v}_{fh})_{\Omega_f} + (q_{fh}, \nabla \cdot \mathbf{u}_{fh})_{\Omega_f} = \langle \mathbf{F}, \underline{\mathbf{v}}_h \rangle_{\mathbf{U}'} \quad (2.11)$$

Theorem 2.2 (Proofs in [21]). *The weak formulation (2.11) of Stokes-Darcy problem is well-posed.*

2.3 Homogenization theory and estimation results for the Darcy region

The Darcy region exhibits multiscale characteristics. In order to better elucidate our model, we introduce the model from [22]

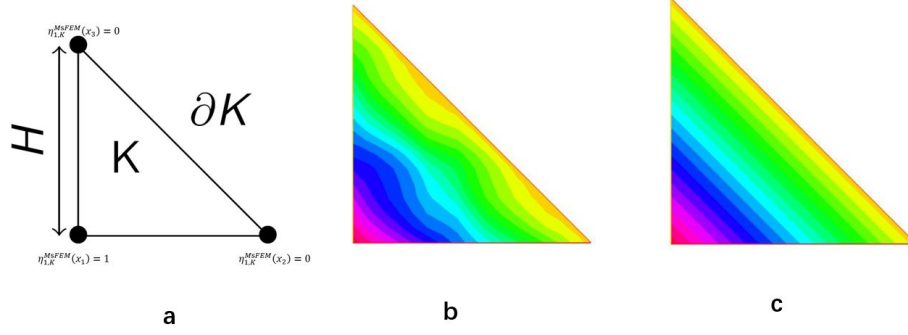


Figure 2: Sketch of MsFEM basis function design in 2D (a), Example of MsFEM basis function (b) and P1 piecewise function (c)

$$\begin{cases} -\operatorname{div}(\mathbb{K}_\epsilon \nabla \phi_p) = f & \text{in } \Omega \\ \phi_p = 0 & \text{on } \Gamma_D \\ \mathbf{n} \cdot \mathbb{K}_\epsilon \nabla \phi_p = g & \text{on } \Gamma_N \end{cases} \quad (2.12)$$

For simplicity, we assume the source term f belongs to $L^2(\Omega)$, and the boundary term $g \in L^2(\Gamma_N)$.

Then, we introduce the multiscale expansion technique in deriving homogenized equations. We look for $\phi_\epsilon(x)$ in the form of asymptotic expansion

$$\phi_\epsilon(x) = \phi_0(x, x/\epsilon) + \epsilon \phi_1(x, x/\epsilon) + \epsilon^2 \phi_2(x, x/\epsilon) + \cdots, \quad (2.13)$$

where the functions $\phi_j(x, y)$ are periodic in y with period 1.

Here, we referenced some definitions and theorems from [22].

Definition 2.1. A (vector/matrix value) function f is called periodic, if $f(\mathbf{x} + \mathbf{z}) = f(\mathbf{x}) \quad \forall \mathbf{x} \in \mathbb{R}^d$ and $\forall \mathbf{z} \in \mathbb{Z}^d$.

We need an interpolation operator. If the triangulation \mathcal{T}_h is regular, then there exist an interpolation operator $\mathcal{I} : H^1(\Omega) \mapsto \mathcal{P}$, $\phi_{\epsilon, \mathcal{I}} \in X_{ph}$.

Theorem 2.3. [Proofs in [22]] Under some assumptions and \mathbb{K}_ϵ is periodic, for (2.12) we have:

$$|\phi_p - \phi_{\epsilon, \mathcal{I}}|_{1, \Omega} \leq C \left\{ \epsilon^{1/2} + h + \sqrt{\frac{\epsilon}{h}} \right\} \|\phi_0\|_{2, \Omega}.$$

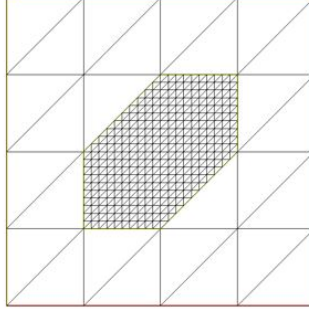
3 Multiscale finite Stokes-Darcy algorithm

In this section, we introduce the algorithm for the multiscale Stokes-Darcy equation. The algorithm is divided into two parts, namely the offline part and the online part. The offline part is used to compute the multiscale basis functions for the Darcy region. The online part utilizes the previously calculated multiscale basis functions and employs the Robin-Robin algorithm to obtain the solution of the equation.

3.1 Offline phase

In the offline phase, we solve the multiscale basis functions in parallel. This approach is adopted to enhance the efficiency of basis function generation.

- The grid is partitioned to obtain the required coarse mesh $K \in \mathcal{T}_h$.

Figure 3: $\mathcal{T}_{h_{finer}}^K$

- For every $K \in \mathcal{T}_h$, we build $\mathcal{T}_{h_{finer}}^K$ and parallelly solve $-\nabla \cdot (\mathbb{K}^\epsilon(x/\epsilon)) \nabla \eta_i = 0$ in $K, \eta_i = \varphi_i$ on ∂K with φ_i the standard P1 basis function and store η_i . See Fig.4.
- Compute and store $A_{i,j}^{loc} = \int_K (\mathbb{K}^\epsilon \nabla \eta_i) (\nabla \eta_j)$ and $B_i = B_i + \int_K \eta_i \times f_p$ with A^{loc} stiffness matrix and B the generic RHS.
- Output: Assemble and store A the stiffness matrix associated with the new basis η_H .

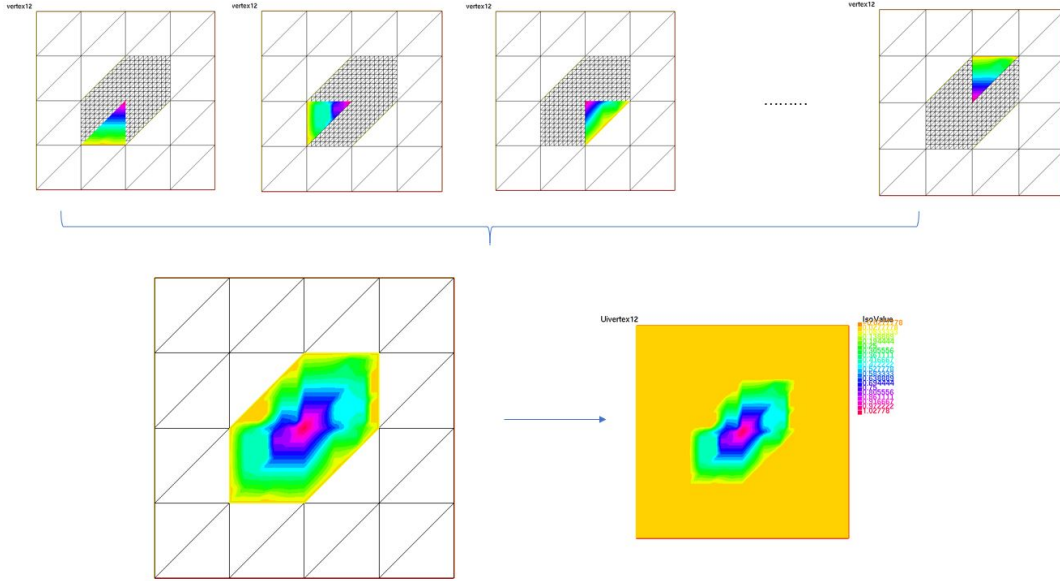


Figure 4: Parallel Efficient Generation of Base Functions

3.2 Online phase

In the online phase, we employ the Robin-Robin Stokes-Darcy algorithm. In this process, we utilize the multiscale basis functions generated in the offline stage. This algorithm is a decoupled algorithm, and here are the main steps:

- Given the initial condtion $\mathbf{u}_f^0, p_f^0, \varphi_p^0, \epsilon_{iter}, \epsilon_{error}, \gamma_f, \gamma_p$.

- For $k = 1, 2, \dots$, independently solve the Stokes and Darcy systems with Robin boundary conditions. More precisely, find $(\mathbf{u}_{fh}^{k+1}, p_{fh}^{k+1})$ such that for all $\mathbf{v}_{fh} \in \mathbf{V}_{fh}$ and $q_{fh} \in Q_{fh}$ it is

$$a_f(\mathbf{u}_{fh}^k, \mathbf{v}_{fh}) + b_f(\mathbf{v}_{fh}, p_{fh}^k) + \gamma_f(\mathbf{u}_{fh}^k \cdot \mathbf{n}_f, \mathbf{v}_{fh} \cdot \mathbf{n}_f) + \alpha(P_\tau \mathbf{u}_{fh}^k, P_\tau \mathbf{v}_{fh}) = (\eta_f^k, \mathbf{v}_{fh} \cdot \mathbf{n}_f) + (\mathbf{g}_f, \mathbf{v}_{fh}),$$

$$b_f(\mathbf{u}_{fh}^k, q_{fh}) = 0.$$

- Find φ_{ph}^{k+1} such that for all $\psi_{ph} \in Q_{ph}$ it is

$$\gamma_p a_p(\phi_{ph}^k, \psi_{ph}) + (g \phi_{ph}^k, \psi_{ph}) = (\eta_p^k, \psi_{ph}) + (g_p, \psi_{ph}).$$

- Update η_p^{k+1} and η_f^{k+1}

$$\eta_f^{k+1} = a\eta_p^k + bg\phi_{ph}^k, \text{ where } a = \frac{\gamma_f}{\gamma_p}, b = -1 - a$$

$$\eta_p^{k+1} = c\eta_f^k + d\mathbf{u}_{fh}^k \cdot \mathbf{n}_f, \text{ where } c = -1, d = \gamma_f + \gamma_p$$

- Compute $\epsilon_{iter} = \|\mathbf{u}_{fh}^{k+1} - \mathbf{u}_{fh}^k\|^2 + \|p_{fh}^{k+1} - p_{fh}^k\|^2 + \|\varphi_{ph}^{k+1} - \varphi_{ph}^k\|^2$
- If $\epsilon_{iter} > \epsilon_{error}$, then $k := k + 1$.
- Output: get the solution $\mathbf{u}_{fh}^N, p_{fh}^N, \varphi_{ph}^N$.

The offline phase involves a parallel method for generating multiscale basis functions. In the online phase, a Robin-Robin online Stokes-Darcy method is employed to obtain the solution. The algorithm offers advantages such as parallel construction of basis functions, which enhances reusability, and ensures high computational accuracy and efficiency. Additionally, the method is easily implementable for generalization and maintenance.

4 Error estimates

In this section, we analyze the error estimate of the above coupled multiscale finite element scheme (2.11). For later analysis, We define the following orthogonal projection P_{fh} from \mathbf{X}_f onto \mathbf{X}_{fh} and ρ_{fh} from Q_f onto Q_{fh} as: for any given $\mathbf{v}_f \in \mathbf{X}_f$ and $p_f \in Q_f$, find $P_{fh}\mathbf{v}_f \in \mathbf{X}_{fh}$ and $\rho_{fh}p_f \in Q_{fh}$ such that

$$2v(\mathbb{D}(\mathbf{v}_f - P_{fh}\mathbf{v}_f), \mathbb{D}(\mathbf{v}_{fh}))_{\Omega_f} + \left(\frac{\alpha v \sqrt{d}}{\sqrt{\text{trace}(\mathbf{\Pi})}} P_\tau(\mathbf{v}_f - P_{fh}\mathbf{v}_f), \mathbf{v}_{fh} \right)_\Gamma + (p_f - \rho_{fh}p_f, \nabla \cdot \mathbf{v}_{fh})_{\Omega_f} = 0 \quad \forall \mathbf{v}_{fh} \in \mathbf{X}_{fh}, \quad (4.1)$$

$$(\nabla \cdot (\mathbf{u}_f - P_{fh}\mathbf{u}_f), q_{fh}) = 0 \quad \forall q_{fh} \in Q_{fh}.$$

For this projection ρ_{fh} and the projection P_{fh} from \mathbf{X}_f onto \mathbf{X}_{fh} in the previous section, we make the following assumption: for any given $\mathbf{v}_f \in \mathbf{H}^2(\Omega_f) \cap \mathbf{X}_f$ and $q_f \in H^1(\Omega_f)$, there holds

$$\|\mathbb{D}(\mathbf{v}_f - P_{fh}\mathbf{v}_f)\|_{\Omega_f} + \|q_f - \rho_{fh}q_f\|_{\Omega_f} \leq ch(\|\mathbf{v}_f\|_{2,\Omega_f} + \|q_f\|_{1,\Omega_f}). \quad (4.2)$$

Suppose the weak solution (\mathbf{u}, p_f) of the mixed Stokes/Darcy problem is local H^2 -regular, that is $\mathbf{u}_f \in \mathbf{H}^2(\Omega_f) \cap \mathbf{V}_f$, $p_f \in H^1(\Omega_f)$, $\phi_p \in H^2(\Omega_p) \cap X_p$ and $\phi_0 \in H^2(\Omega_p) \cap X_p$

Theorem 4.1 (H^1 norm). Assume that \mathbb{K}_ϵ is periodic, uniformly elliptic and symmetric. Let Ω be a bounded Lipschitz domain in \mathbb{R}^2 , and let (\mathbf{u}_f, ϕ_p) and $(\mathbf{u}_{fh}, \phi_{ph})$ be the solutions of Problems (2.8) and (2.11), respectively.

$$\begin{aligned} \sqrt{\nu} \|\mathbb{D}(\mathbf{u}_f - \mathbf{u}_{fh})\|_{\Omega_f} + \frac{\sqrt{g}}{2} \left\| \mathbb{K}_\epsilon^{\frac{1}{2}} \nabla(\phi_p - \phi_{ph}) \right\|_{\Omega_p} &\leq \hat{C}_1 \left\{ \epsilon^{1/2} + h + \sqrt{\frac{\epsilon}{h}} \right\} \|\phi_0\|_{2, \Omega_p} \\ &\quad + \hat{C}_2 h (\|\mathbf{u}_f\|_{2, \Omega_f} + \|p_f\|_{1, \Omega_f}), \end{aligned} \quad (4.3)$$

where \hat{C}_1, \hat{C}_2 depends on $\lambda_{\max}, \lambda_{\min}, g, \nu$.

If we denote

$$\begin{aligned} \mathbf{u}_f - \mathbf{u}_{fh} &= (\mathbf{u}_f - P_{fh}\mathbf{u}_f) + (P_{fh}\mathbf{u}_f - \mathbf{u}_{fh}) = \hat{\mathbf{e}}_f + \mathbf{e}_{fh}, \\ \phi_p - \phi_{ph} &= (\phi_p - \phi_{\epsilon, \mathcal{I}}) + (\phi_{\epsilon, \mathcal{I}} - \phi_{ph}) = \hat{e}_p + e_{ph}, \\ p_f - p_{fh} &= (p_f - \rho_{fh}p_f) + (\rho_{fh}p_f - p_{fh}) = \hat{e}_\theta + e_\theta. \end{aligned}$$

Proof. Recall the weak formulation and its finite element scheme

$$\begin{cases} a(\underline{\mathbf{u}}, \underline{\mathbf{v}}) - (p_f, \nabla \cdot \mathbf{v}_f)_{\Omega_f} = \langle F, \underline{\mathbf{v}} \rangle, & \forall (\underline{\mathbf{v}}, q_f) \in \mathbf{U} \times Q_f, \\ (q_f, \nabla \cdot \mathbf{u}_f)_{\Omega_f} = 0, & \forall q_f \in Q_f. \end{cases} \quad (4.4)$$

$$\begin{cases} a(\underline{\mathbf{u}}_h, \underline{\mathbf{v}}_h) - (p_{fh}, \nabla \cdot \mathbf{v}_{fh})_{\Omega_f} + (q_{fh}, \nabla \cdot \mathbf{u}_{fh})_{\Omega_f} = \langle F, \underline{\mathbf{v}}_h \rangle & \forall (\underline{\mathbf{v}}_h, q_{fh}) \in \mathbf{U}_h \times Q_{fh}, \\ (q_{fh}, \nabla \cdot \mathbf{u}_{fh})_{\Omega_f} = 0, & \forall q_{fh} \in Q_{fh}. \end{cases}$$

where

$$\begin{aligned} a(\underline{\mathbf{u}}, \underline{\mathbf{v}}) &= 2\nu (\mathbb{D}(\mathbf{u}_f), \mathbb{D}(\mathbf{v}_f))_{\Omega_f} + g(\phi_p, \mathbf{v}_f \cdot \mathbf{n}_f)_\Gamma \\ &\quad + \left(\frac{\alpha v \sqrt{d}}{\sqrt{\text{trace}(\mathbf{\Pi})}} P_\tau(\mathbf{u}_f), \mathbf{v}_f \right)_\Gamma \\ &\quad + g(\mathbb{K} \nabla \phi_p, \nabla \psi_p)_{\Omega_p} - g(\psi_p, \mathbf{u}_f \cdot \mathbf{n}_f)_\Gamma \end{aligned} \quad (4.5)$$

Then,

$$\begin{aligned} &2\nu (\mathbb{D}(\mathbf{u}_f - \mathbf{u}_{fh}), \mathbb{D}(\mathbf{v}_{fh}))_{\Omega_f} + g(\phi_p - \phi_{ph}, \mathbf{v}_{fh} \cdot \mathbf{n}_f)_\Gamma \\ &\quad + \left(\frac{\alpha v \sqrt{d}}{\sqrt{\text{trace}(\mathbf{\Pi})}} P_\tau(\mathbf{u}_f - \mathbf{u}_{fh}), \mathbf{v}_{fh} \right)_\Gamma \\ &\quad + g(\mathbb{K} \nabla(\phi_p - \phi_{ph}), \nabla \psi_{ph})_{\Omega_p} - g(\psi_{ph}, \mathbf{u}_f \cdot \mathbf{n}_f - \mathbf{u}_{fh} \cdot \mathbf{n}_{fh})_\Gamma \\ &\quad - (p_f - p_{fh}, \nabla \cdot \mathbf{v}_{fh})_{\Omega_f} + (q_{fh}, \nabla \cdot (\mathbf{u}_f - \mathbf{u}_{fh}))_{\Omega_f} = 0. \end{aligned} \quad (4.6)$$

Using (4.1) and (4.4), it deduces:

$$\begin{aligned} &2\nu (\mathbb{D}(\mathbf{e}_{fh}), \mathbb{D}(\mathbf{v}_{fh}))_{\Omega_f} + g(\hat{e}_p + e_{ph}, \mathbf{v}_{fh} \cdot \mathbf{n}_f)_\Gamma \\ &\quad + \left(\frac{\alpha v \sqrt{d}}{\sqrt{\text{trace}(\mathbf{\Pi})}} P_\tau(\mathbf{e}_{fh}), \mathbf{v}_{fh} \right)_\Gamma \\ &\quad + g(\mathbb{K} \nabla(\hat{e}_p + e_{ph}), \nabla \psi_{ph})_{\Omega_p} - g(\psi_{ph}, (\hat{\mathbf{e}}_f + \mathbf{e}_{fh}) \cdot \mathbf{n}_f)_\Gamma = 0. \end{aligned} \quad (4.7)$$

Taking $\mathbf{v}_{fh} = \mathbf{e}_{fh}, \psi_{ph} = e_{ph}$ into (4.7), we can get

$$\begin{aligned} &2\nu (\mathbb{D}(\mathbf{e}_{fh}), \mathbb{D}(\mathbf{e}_{fh}))_{\Omega_f} + g(\hat{e}_p + e_{ph}, \mathbf{e}_{fh} \cdot \mathbf{n}_f)_\Gamma \\ &\quad + \left(\frac{\alpha v \sqrt{d}}{\sqrt{\text{trace}(\mathbf{\Pi})}} P_\tau(\mathbf{e}_{fh}), \mathbf{e}_{fh} \right)_\Gamma \\ &\quad + g(\mathbb{K} \nabla(\hat{e}_p + e_{ph}), \nabla e_{ph})_{\Omega_p} - g(e_{ph}, (\hat{\mathbf{e}}_f + \mathbf{e}_{fh}) \cdot \mathbf{n}_f)_\Gamma = 0. \end{aligned} \quad (4.8)$$

Then

$$\begin{aligned}
& 2\nu (\mathbb{D}(\mathbf{e}_{fh}), \mathbb{D}(\mathbf{e}_{fh}))_{\Omega_f} + g(e_{ph}, \mathbf{e}_{fh} \cdot \mathbf{n}_f)_{\Gamma} \\
& + \left(\frac{\alpha v \sqrt{d}}{\sqrt{\text{trace}(\mathbf{\Pi})}} P_{\tau}(\mathbf{e}_{fh}), \mathbf{e}_{fh} \right)_{\Gamma} \\
& + g(\mathbb{K} \nabla(e_{ph}), \nabla e_{ph})_{\Omega_p} - g(e_{ph}, (\mathbf{e}_{fh}) \cdot \mathbf{n}_f)_{\Gamma} \\
& = -g(\hat{e}_p, \mathbf{e}_{fh} \cdot \mathbf{n}_f)_{\Gamma} - g(\mathbb{K} \nabla(\hat{e}_p), \nabla e_{ph})_{\Omega_p} + g(e_{ph}, \hat{\mathbf{e}}_f \cdot \mathbf{n}_f)_{\Gamma}.
\end{aligned} \tag{4.9}$$

and we can get

$$\begin{aligned}
& 2\nu \|\mathbb{D}(\mathbf{e}_{fh})\|_{\Omega_f}^2 + \frac{g}{2} \left\| \mathbb{K}^{\frac{1}{2}} \nabla e_{ph} \right\|_{\Omega_p}^2 + \underbrace{\left(\frac{\alpha v \sqrt{d}}{\sqrt{\text{trace}(\mathbf{\Pi})}} P_{\tau}(\mathbf{e}_{fh}), \mathbf{e}_{fh} \right)_{\Gamma}}_{\textcircled{1}} \\
& \leq \underbrace{|g(\hat{e}_p, \mathbf{e}_{fh} \cdot \mathbf{n}_f)_{\Gamma}|}_{\textcircled{2}} + \underbrace{|g(\mathbb{K} \nabla(\hat{e}_p), \nabla e_{ph})_{\Omega_p}|}_{\textcircled{3}} + \underbrace{|g(e_{ph}, \hat{\mathbf{e}}_f \cdot \mathbf{n}_f)_{\Gamma}|}_{\textcircled{4}}
\end{aligned} \tag{4.10}$$

For $\textcircled{1}$:

$$\begin{aligned}
\left(\frac{\alpha v \sqrt{d}}{\sqrt{\text{trace}(\mathbf{\Pi})}} P_{\tau}(\mathbf{e}_{fh}), \mathbf{e}_{fh} \right)_{\Gamma} & = \left(\frac{\alpha v \sqrt{d}}{\sqrt{\text{trace}(\mathbf{\Pi})}} (\mathbf{e}_{fh} \cdot \tau), \mathbf{e}_{fh} \cdot \tau \right)_{\Gamma} \\
& = \frac{\alpha v \sqrt{d}}{\sqrt{\text{trace}(\mathbf{\Pi})}} \|\mathbf{e}_{fh} \cdot \tau\|_{\Gamma}^2 \geq 0.
\end{aligned} \tag{4.11}$$

Then, we estimate the three terms on the right hand side of the above inequality.

For $\textcircled{2}$:

$$\begin{aligned}
|g(\hat{e}_p, \mathbf{e}_{fh} \cdot \mathbf{n}_f)_{\Gamma}| & \leq g \|\hat{e}_p\|_{L^2(\Gamma)} \|\mathbf{e}_{fh}\|_{\mathbf{L}^2(\Gamma)} \leq Cg \|\nabla \hat{e}_p\|_{\Omega_p} \|\mathbb{D}(\mathbf{e}_{fh})\|_{\Omega_f} \\
& \leq \frac{C^2 g^2}{4\nu} \|\nabla \hat{e}_p\|_{\Omega_p}^2 + \nu \|\mathbb{D}(\mathbf{e}_{fh})\|_{\Omega_f}^2.
\end{aligned} \tag{4.12}$$

For $\textcircled{3}$:

$$\begin{aligned}
|g(\mathbb{K} \nabla(\hat{e}_p), \nabla e_{ph})_{\Omega_p}| & \leq g \lambda_{\max}^{\frac{1}{2}} \|\nabla \hat{e}_p\|_{\Omega_p} \left\| \mathbb{K}^{\frac{1}{2}} \nabla e_{ph} \right\|_{\Omega_p} \\
& \leq g \lambda_{\max}^{\frac{1}{2}} \|\nabla \hat{e}_p\|_{\Omega_p} \left\| \mathbb{K}^{\frac{1}{2}} \nabla e_{ph} \right\|_{\Omega_p} \\
& \leq 2g \lambda_{\max} \|\nabla \hat{e}_p\|_{\Omega_p}^2 + \frac{g}{8} \left\| \mathbb{K}^{\frac{1}{2}} \nabla e_{ph} \right\|_{\Omega_p}^2.
\end{aligned} \tag{4.13}$$

For $\textcircled{4}$:

$$\begin{aligned}
|g(e_{ph}, \hat{\mathbf{e}}_f \cdot \mathbf{n}_f)_{\Gamma}| & \leq g \|e_{ph}\|_{\Gamma} \|\hat{\mathbf{e}}_f \cdot \mathbf{n}_f\|_{\Gamma} \\
& \leq \frac{gC}{\lambda_{\min}^{\frac{1}{2}}} \left\| \mathbb{K}^{\frac{1}{2}} \nabla e_{ph} \right\|_{\Omega_p} \|\hat{\mathbf{e}}_f\|_{1, \Omega_f} \\
& \leq \frac{g}{8} \left\| \mathbb{K}^{\frac{1}{2}} \nabla e_{ph} \right\|_{\Omega_p}^2 + \frac{2gC^2}{\lambda_{\min}} \|\hat{\mathbf{e}}_f\|_{1, \Omega_f}^2.
\end{aligned} \tag{4.14}$$

Combining the above bounds and using (4.2) and Theorem 2.3, it yields

$$\begin{aligned}
\nu \|\mathbb{D}(\mathbf{u}_f - \mathbf{u}_{fh})\|_{\Omega_f}^2 + \frac{g}{4} \left\| \mathbb{K}_{\epsilon}^{\frac{1}{2}} \nabla(\phi_p - \phi_{ph}) \right\|_{\Omega_p}^2 & \leq \left(\frac{C^2 g^2}{4\nu} + 2g \lambda_{\max} \right) \left\{ \epsilon^{1/2} + h + \sqrt{\frac{\epsilon}{h}} \right\}^2 \|\phi_0\|_{2, \Omega_p}^2 \\
& + \frac{2g}{\lambda_{\min}} C h^2 (\|\mathbf{u}_f\|_{2, \Omega_f} + \|p_f\|_{1, \Omega_f})^2.
\end{aligned} \tag{4.15}$$

Then, it is easily get the final result (4.3).

□

Remark 4.1. Given that $\|\mathbf{u}_f\|_{2,\Omega_f}$, $\|p_f\|_{1,\Omega_f}$ and $\|\phi_0\|_{2,\Omega_p}$ are bounded, the H^1 norm can be controlled by $\epsilon^{1/2} + h + \sqrt{\frac{\epsilon}{h}}$.

Let us introduce the formal adjoint problem ([15]): find $\underline{\mathbf{w}} = (\mathbf{w}_f, \xi_p) \in \mathbf{V}$ such that

$$a(\underline{\mathbf{v}}, \underline{\mathbf{w}}) = (f, \underline{\mathbf{v}}) \quad \forall \underline{\mathbf{v}} = (\mathbf{v}_f, \psi_p) \in \mathbf{V}, \quad (4.16)$$

where $f := (\mathbf{u}_f - \mathbf{u}_{fh}, \phi_p - \phi_{ph})$.

$$a(\underline{\mathbf{v}}, \underline{\mathbf{w}}) = (\mathbf{u}_f - \mathbf{u}_{fh}, \mathbf{v}_f)_{\Omega_f} + g(\phi_p - \phi_{ph}, \psi_p)_{\Omega_p} \quad \forall \underline{\mathbf{v}} = (\mathbf{v}_f, \psi_p) \in \mathbf{V}. \quad (4.17)$$

We assume that $\underline{\mathbf{w}}$ has the regularity estimate:

$$\|\underline{\mathbf{w}}\|_{H^2} \leq C_R \|f\|_{L^2}, \quad (4.18)$$

and

$$\|\underline{\mathbf{w}}_0\|_{H^2} \leq C_R \|f\|_{L^2}, \quad (4.19)$$

where $\underline{\mathbf{w}}_0 = (\mathbf{w}_f, \xi_{p,0})$ and $\xi_{p,0}$ is the $O(\epsilon^0)$ asymptotic expansion of ξ_p .

Theorem 4.2 (L2 norm). Assume that \mathbb{K}^ϵ is periodic, uniformly elliptic and symmetric. Let Ω be a bounded Lipschitz domain in \mathbb{R}^2 , and let (\mathbf{u}_f, ϕ_p) and $(\mathbf{u}_{fh}, \phi_{ph})$ be the solutions of Problems (2.8) and (2.11), respectively.

$$\begin{aligned} \|(\mathbf{u}_f - \mathbf{u}_{fh})\|_{\Omega_f} + g\|(\phi_p - \phi_{ph})\|_{\Omega_p} &\leq \tilde{C}_1 \left\{ \epsilon + h^2 + \frac{\epsilon}{h} \right\} \|\phi_0\|_{2,\Omega} \\ &\quad + \tilde{C}_2 \left(h^2 + \sqrt{\epsilon h} \right) (\|\mathbf{u}_f\|_{2,\Omega_f} + \|p_f\|_{1,\Omega_f}), \end{aligned} \quad (4.20)$$

where \tilde{C}_1, \tilde{C}_2 depends on $\lambda_{\max}, \lambda_{\min}, g, \nu$.

Proof.

$$\begin{aligned} \|\underline{\mathbf{u}} - \underline{\mathbf{u}}_h\|_{\Omega}^2 &= (\mathbf{u} - \mathbf{u}_h, \mathbf{u} - \mathbf{u}_h)_{\Omega_f} + g(\phi_p - \phi_{ph}, \phi_p - \phi_{ph})_{\Omega_p} \\ &= a(\underline{\mathbf{u}} - \underline{\mathbf{u}}_h, \underline{\mathbf{w}}) \\ &= a(\underline{\mathbf{u}} - \underline{\mathbf{u}}_h, \underline{\mathbf{w}} - \mathcal{I}^h \underline{\mathbf{w}}) \\ &\leq C \|\underline{\mathbf{u}} - \underline{\mathbf{u}}_h\|_{1,\Omega} \|\underline{\mathbf{w}} - \mathcal{I}^h \underline{\mathbf{w}}\|_{H^1(\Omega)} \\ &\leq C \|\underline{\mathbf{u}} - \underline{\mathbf{u}}_h\|_{1,\Omega} \sqrt{((\nabla(w_f - \mathcal{I}^h w_f), \nabla(w_f - \mathcal{I}^h w_f)) + g(\mathbb{K} \nabla(\xi_p - \mathcal{I}^h \xi_p), \nabla(\xi_p - \mathcal{I}^h \xi_p)))} \\ &\leq C_1 \|\underline{\mathbf{u}} - \underline{\mathbf{u}}_h\|_{1,\Omega} \left[\|w_f - \mathcal{I}^h w_f\|_{1,\Omega_f} + \sqrt{g} \lambda_{\max}^{\frac{1}{2}} \|\xi_p - \mathcal{I}^h \xi_p\|_{1,\Omega_p} \right] \\ &\leq C_2 \|\underline{\mathbf{u}} - \underline{\mathbf{u}}_h\|_{1,\Omega} \left[h \|w_f\|_{2,\Omega_f} + \sqrt{g} \lambda_{\max}^{\frac{1}{2}} \left(\epsilon^{\frac{1}{2}} + h + \sqrt{\frac{\epsilon}{h}} \right) \|\xi_{p,0}\|_{2,\Omega_p} \right] \\ &\leq C_3 \|\underline{\mathbf{u}} - \underline{\mathbf{u}}_h\|_{1,\Omega} \left(\epsilon^{\frac{1}{2}} + h + \sqrt{\frac{\epsilon}{h}} \right) (\|w_f\|_{2,\Omega_f} + \|\xi_{p,0}\|_{2,\Omega_p}) \\ &\leq C_3 \|\underline{\mathbf{u}} - \underline{\mathbf{u}}_h\|_{1,\Omega} \left(\epsilon^{\frac{1}{2}} + h + \sqrt{\frac{\epsilon}{h}} \right) \|\underline{\mathbf{u}} - \underline{\mathbf{u}}_h\|_{\Omega}. \end{aligned} \quad (4.21)$$

Therefore,

$$\|\underline{\mathbf{u}} - \underline{\mathbf{u}}_h\|_{\Omega} \leq C_3 \|\underline{\mathbf{u}} - \underline{\mathbf{u}}_h\|_{1,\Omega} \left(\epsilon^{\frac{1}{2}} + h + \sqrt{\frac{\epsilon}{h}} \right). \quad (4.22)$$

Using Theorem 4.1, it yields the final result (4.20) \square

Remark 4.2. Given that $\|\mathbf{u}_f\|_{2,\Omega_f}$, $\|p_f\|_{1,\Omega_f}$ and $\|\phi_0\|_{2,\Omega_p}$ are bounded, the L^2 norm can be controlled by $\epsilon + h^2 + \frac{\epsilon}{h}$.

5 Numerical experiments

In this section, we study the accuracy of the multiscale method through numerical computations. The model problem is solved using the multiscale method with base functions defined by linear condition (MsFem). Since it is very difficult to construct a test problem with exact solution and sufficient generality, we use resolved numerical solutions in place of exact solutions. The numerical results are compared with the theoretical analysis. Additionally, we present a numerical example illustrating the method's application to more complex problems involving separable scales, nonseparable scales and high-contrast case.

5.1 Implementation

We outline the implementation here and define some notation to be frequently used below. For convenience, we assume that the multiscale Darcy region is situated on the unit square. Let N be the number of elements in the x and y directions. The size of mesh is thus $h = 1/N$. To compute the base functions, each element is discretized into $M \times M$ subcell elements with size $h_{finer} = h/M$. Triangular elements are used in all numerical tests.

In the offline phase, we utilize P1 elements to compute basis functions within each element. During this process, the Message Passing Interface (MPI) is employed to enhance efficiency, and the stiffness matrix and right-hand side are stored for subsequent online computations.

Because it is very difficult to construct a genuine 2D steady Stokes-Darcy model with an exact solution, reference solutions are used as the exact solutions for the test problems. In all numerical examples below, the resolved solutions are obtained using standard FEM. We use the numerical computation libraries MUMPS and PETSc within FreeFEM++ to calculate the reference solution. Due to the multiscale nature of the permeability in our Darcy region, we employ a finer mesh within the Darcy region when computing the reference solution. We have computed a reference solution of this numerical example using Talor-Hood finite element and P2 element with a mesh of size $H_D = 1/2048$ (in Darcy region), $H_S = 1/512$ (in Stokes region). The purpose of computing the reference solution is to obtain the error. To enhance computational speed, we utilize a domain decomposition parallel approach for computing the reference solution. We define the reference solution $\mathbf{u}^{\text{reference}} = (\mathbf{u}_f^{\text{reference}}, \phi_p^{\text{reference}})$.

To facilitate the comparison among different schemes, we use the following shorthands: FEM-FEM stands for MINI elements in the Stokes region and P1 elements in the Darcy region and FEM-MsFEM stands for MINI elements in the Stokes region and multiscale basis function in the Darcy region. We define the numerical solution $\mathbf{u}^{\text{numerical}} = (\mathbf{u}_f^{\text{numerical}}, \phi_p^{\text{numerical}})$.

5.2 Numerical result

We define some norms to demonstrate the error.

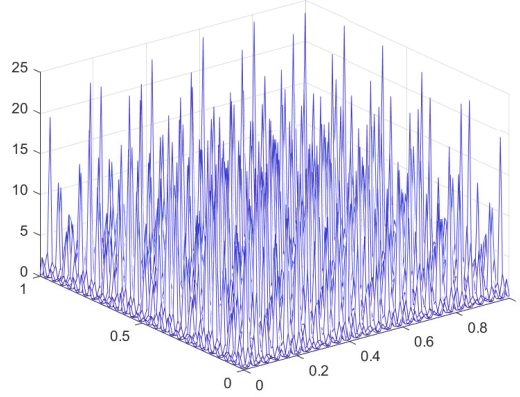
$$\begin{aligned} \|e_{\mathbf{u}_f}\|_{L^2} &= \|\mathbf{u}_f^{\text{reference}} - \mathbf{u}_f^{\text{numerical}}\|_{L^2(\Omega_f)}, \|e_{\mathbf{u}_f}\|_{H^1} = \|\mathbf{u}_f^{\text{reference}} - \mathbf{u}_f^{\text{numerical}}\|_{H^1(\Omega_f)} \\ \|e_{\phi_p}\|_{L^2} &= \|\phi_p^{\text{reference}} - \phi_p^{\text{numerical}}\|_{H^1(\Omega_p)}, \|e_{\phi_p}\|_{L^2} = \|\phi_p^{\text{reference}} - \phi_p^{\text{numerical}}\|_{H^1(\Omega_p)} \end{aligned}$$

5.2.1 Example 1

In this example, we consider nonseparable scales and solve (2.3) with

$$\mathbb{K}_\epsilon = \frac{1}{(2 + P \sin(2\pi x/\epsilon))(2 + P \sin(2\pi y/\epsilon))},$$

where P is a parameter controlling the magnitude of the oscillation. We take $P = 1.8$ in this example. The right hand side function $\mathbf{g}_f(x, y), g_p(x, y)$ is zero. On $\partial\Omega_p$, we impose $\phi = 0$ and on the $\partial\Omega_f$, $u_f = [\sin(\pi x), 0]$, on $(0, 1) \times \{2\}$, $u_f = [0, 0]$, on $\{0\} \times (1, 2) \cup \{1\} \times (1, 2)$. We set all physical parameters ν, α, g equal to 1. The Robin-Robin coefficients are set to $\gamma_f = 0.1, \gamma_p = 1$.

Figure 5: \mathbb{K}_ϵ in Example 1

The result of FEM-MsFEM error with varying h but fixed $\epsilon = 0.008$ and $h_{finer} = 1/2048$ are shown in Table 1. When observing the errors in the Darcy part, we first fix the small parameter ϵ and gradually refine the grid. As h decreases and $h \gg \epsilon$, we can observe that the convergence order of the L^2 error for e_{ϕ_p} degrades from around +2 to around -1. This effectively validates the term $O(h^2)$ to $O(\epsilon/h)$ in the L^2 error analysis. Additionally, the convergence order of the H^1 error degrades from +1 to -0.5, providing a good validation of the term $O(h)$ to $O(\sqrt{\epsilon/h})$ in the L^2 error analysis. Furthermore, when observing the errors $e_{\mathbf{u}_f}$ in the Stokes part, we use standard MINI elements in the Stokes region. However, it can be seen that the L^2 error in Stokes does not initially reach the optimal order of 2, and with the gradual decrease in grid size h , the convergence order of the Stokes L^2 error also shows a decreasing trend. The reason for this decrease is influenced by the Darcy region, as the Darcy region also experiences a reduction in order at this point in time. Next, when observing the order of the velocity H^1 , it can be noted that the H^1 order does not initially reach the optimal order, but with a decrease in h , the H^1 error order remains almost constant.

The result of FEM-FEM error with varying h but fixed $\epsilon = 0.008$ are shown in Table 2. When observing errors in the Darcy part, we first fix the small parameter ϵ . As h decreases and $h \gg \epsilon$, we can observe that the convergence orders of the L^2 error and H^1 error for pressure become unstable. Comparing with Table 1, it is noticeable that for $h \gg \epsilon$, the error accuracy of FEM-MsFEM is higher than that of FEM-FEM. For instance, when $h = 1/16$, the accuracy of e_{ϕ_p} in the FEM-MsFEM algorithm can reach 10^{-5} , whereas FEM-FEM can only achieve 10^{-4} . When observing errors in the Stokes part, it can be noted that FEM-FEM does not reach the optimal order, and with the decrease in grid size h , the convergence order of the Stokes L^2 error also shows a decreasing trend. The order of H^1 does not initially reach the optimal order, but with a decrease in h , the H^1 error order remains almost constant. This result is consistent with the situation in FEM-MsFEM and is influenced by the Darcy region.

FEM-MsFEM error at $\frac{\epsilon}{h} = 0.32$, $N = 32$, are shown in Table 3. Our main goal is to observe errors in FEM-MsFEM when fixing ϵ/h , where $h_{finer} = h/N$. In the Darcy part, as h gradually decreases, it can be observed that the L^2 and H^1 errors remain almost constant. This validates the importance of $O(\epsilon/h)$ in the L^2 error and $O(\sqrt{\epsilon/h})$ in the H^1 error. In the Stokes region, the convergence orders of L^2 and H^1 errors fail to reach the optimal order, and there is no significant change in the orders.

5.2.2 Example 2

In this example, we consider nonseparable scales and solve (2.3) with

$$\mathbb{K}_\epsilon = \frac{1}{4 + P(\sin(2\pi x/\epsilon) + \sin(2\pi y/\epsilon))},$$

Table 1: FEM-MsFEM error with varying h but fixed $\epsilon = 0.008$ and $h_{finer} = 1/2048$.

h	$\ e_{\mathbf{u}_f}\ _{L^2}$	Order	$\ e_{u_f}\ _{H^1}$	Order	$\ e_{\phi_p}\ _{L^2}$	Order	$\ e_{\phi_p}\ _{H^1}$	Order
1/4	6.07E-02		1.67E+00		8.99E-04		1.67E-02	
1/8	1.80E-02	1.76	9.44E-01	0.82	1.97E-04	2.19	7.56E-03	1.14
1/16	4.79E-03	1.91	5.07E-01	0.90	8.43E-05	1.23	4.82E-03	0.65
1/32	1.27E-03	1.92	2.69E-01	0.92	1.75E-04	-1.05	5.05E-03	-0.07
1/64	3.43E-04	1.89	1.41E-01	0.93	3.25E-04	-0.89	6.82E-03	-0.44
1/128	1.22E-04	1.49	7.41E-02	0.93	5.56E-04	-0.78	9.47E-03	-0.47
1/256	5.79E-05	1.07	3.85E-02	0.95	3.79E-04	0.55	7.85E-03	0.27

Table 2: FEM-FEM error with varying h but fixed $\epsilon = 0.008$.

h	$\ e_{\mathbf{u}_f}\ _{L^2}$	Order	$\ e_{u_f}\ _{H^1}$	Order	$\ e_{\phi_p}\ _{L^2}$	Order	$\ e_{\phi_p}\ _{H^1}$	Order
1/4	6.07E-02		1.67E+00		5.31E-04		1.44E-02	
1/8	1.80E-02	1.76	9.44E-01	0.82	9.33E-04	-0.81	1.34E-02	0.10
1/16	4.81E-03	1.90	5.07E-01	0.90	8.61E-04	0.12	1.26E-02	0.09
1/32	1.28E-03	1.91	2.69E-01	0.92	9.03E-04	-0.07	1.27E-02	-0.01
1/64	3.62E-04	1.83	1.41E-01	0.93	7.89E-04	0.19	1.19E-02	0.09
1/128	1.55E-04	1.22	7.41E-02	0.93	8.76E-04	-0.15	1.23E-02	-0.04
1/256	7.20E-05	1.11	3.85E-02	0.95	4.81E-04	0.86	8.73E-03	0.49

where P is a parameter controlling the magnitude of the oscillation. We take $P = 1.5$ in this example. The right hand side function $\mathbf{g}_f(x, y)$, $g_p(x, y)$ is zero

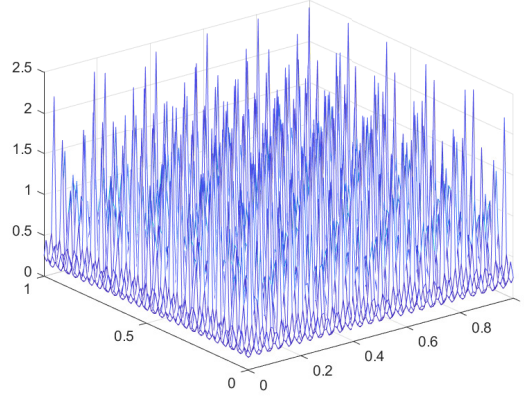
On $\partial\Omega_p$, we impose $\phi = 0$ and on the $\partial\Omega_f$, $u_f = [\sin(\pi x), 0]$, on $(0, 1) \times \{2\}$, $u_f = [0, 0]$, on $\{0\} \times (1, 2) \cup \{1\} \times (1, 2)$. We set all physical parameters ν, α, g equal to 1. The Robin-Robin coefficients are set to $\gamma_f = 0.1, \gamma_p = 1$.

The result of FEM-MsFEM error with varying h but fixed $\epsilon = 0.008$ and $h_{finer} = 1/2048$ are shown in Table 4. When examining errors in the Darcy part, we initially set a fixed small parameter and progressively refine the grid. As h decreases, with $h \gg \epsilon$, we observe a degradation in the convergence order of the L^2 error for e_{ϕ_p} from around +2 to approximately -1. This observation effectively confirms the presence of terms $O(h^2)$ to $O(\epsilon/h)$ in the L^2 error analysis. Additionally, the convergence order of the H^1 error decreases from +1 to -0.5, providing robust validation for terms $O(h)$ to $O(\sqrt{\epsilon/h})$ in the L^2 error analysis. Moreover, when evaluating errors $e_{\mathbf{u}_f}$ in the Stokes part, standard MINI elements are employed in the Stokes region. However, it is evident that the L^2 error in Stokes does not initially attain the optimal order of 2. As the grid size h gradually decreases, the convergence order of the Stokes L^2 error exhibits a declining trend. This decline is attributed to the influence of the Darcy region. Subsequently, when inspecting the order of the velocity H^1 , it is observed that the H^1 order does not initially reach the optimal level, yet with a decrease in h , the H^1 error order remains relatively constant.

The result of FEM-FEM error with varying h but fixed $\epsilon = 0.008$ in Table 5. When observing errors

Table 3: FEM-MsFEM error at $\frac{\epsilon}{h} = 0.32$, $N = 32$.

h	ϵ	$\ e_{u_p}\ _{L^2}$	Order	$\ e_{u_f}\ _{H^1}$	Order	$\ e_{\phi_p}\ _{L^2}$	Order	$\ e_{\phi_p}\ _{H^1}$	Order
1/16	0.02	4.80E-03		5.07E-01		3.05E-04		6.89E-03	
1/32	0.01	1.27E-03	1.92	2.69E-01	0.92	2.88E-04	0.08	5.99E-03	0.20
1/64	0.005	3.38E-04	1.91	1.41E-01	0.93	2.80E-04	0.04	5.76E-03	0.06
1/128	0.0025	9.71E-05	1.80	7.41E-02	0.93	2.71E-04	0.05	5.63E-03	0.03

Figure 6: \mathbb{K}_ϵ in Example 2

in the Darcy part, we first fix the small parameter ϵ . As h decreases and $h \gg \epsilon$, we can observe that the convergence orders of the L^2 error and H^1 error for pressure become unstable. Comparing with Table 4, it is noticeable that for $h \gg \epsilon$, the error accuracy of FEM-MsFEM is higher than that of FEM-FEM. For instance, when $h = 1/16$, the accuracy of e_{ϕ_p} in the FEM-MsFEM algorithm can reach 10^{-5} , whereas FEM-FEM can only achieve 10^{-4} . When observing errors in the Stokes part, it can be noted that FEM-FEM does not reach the optimal order, and with the decrease in grid size h , the convergence order of the Stokes L^2 error also shows a decreasing trend. The order of H^1 does not initially reach the optimal order, but with a decrease in h , the H^1 error order remains almost constant. This result is consistent with the situation in FEM-MsFEM and is influenced by the Darcy region.

FEM-MsFEM error at $\frac{\epsilon}{h} = 0.32$, $N = 32$, are shown in Table 6. Our main goal is to observe errors in FEM-MsFEM when fixing ϵ/h , where $h_{finer} = h/N$. In the Darcy part, as h gradually decreases, it can be observed that the L^2 and H^1 errors remain almost constant. This validates the importance of $O(\epsilon/h)$ in the L^2 error and $O(\sqrt{\epsilon/h})$ in the H^1 error. In the Stokes region, the convergence orders of L^2 and H^1 errors fail to reach the optimal order, and there is no significant change in the orders.

Table 4: FEM-MsFEM error with varying h but fixed $\epsilon = 0.008$ and $h_{finer} = 1/2048$.

h	$\ e_{\mathbf{u}_f}\ _{L^2}$	Order	$\ e_{u_f}\ _{H^1}$	Order	$\ e_{\phi_p}\ _{L^2}$	Order	$\ e_{\phi_p}\ _{H^1}$	Order
1/4	6.07E-02		1.67E+00		2.00E-03		3.12E-02	
1/8	1.80E-02	1.76	9.44E-01	0.82	5.06E-04	1.98	1.36E-02	1.20
1/16	4.79E-03	1.91	5.07E-01	0.90	8.65E-05	2.55	6.93E-03	0.97
1/32	1.26E-03	1.92	2.69E-01	0.92	6.31E-05	0.45	5.08E-03	0.45
1/64	3.34E-04	1.92	1.41E-01	0.93	1.23E-04	-0.96	5.89E-03	-0.21
1/128	9.44E-05	1.82	7.41E-02	0.93	2.28E-04	-0.90	7.94E-03	-0.43
1/256	3.28E-05	1.53	3.85E-02	0.95	1.70E-04	0.43	6.75E-03	0.23

Table 5: FEM-FEM error with varying h but fixed $\epsilon = 0.008$.

h	$\ e_{\mathbf{u}_f}\ _{L^2}$	Order	$\ e_{u_f}\ _{H^1}$	Order	$\ e_{\phi_p}\ _{L^2}$	Order	$\ e_{\phi_p}\ _{H^1}$	Order
1/4	6.07E-02		1.67E+00		1.68E-03		2.91E-02	
1/8	1.80E-02	1.76	9.44E-01	0.82	4.96E-04	1.76	1.53E-02	0.93
1/16	4.80E-03	1.91	5.07E-01	0.90	3.30E-04	0.59	1.17E-02	0.39
1/32	1.27E-03	1.92	2.69E-01	0.92	4.21E-04	-0.35	1.07E-02	0.13
1/64	3.37E-04	1.92	1.41E-01	0.93	2.68E-04	0.65	9.88E-03	0.11
1/128	1.03E-04	1.70	7.41E-02	0.93	3.69E-04	-0.46	1.00E-02	-0.02
1/256	3.73E-05	1.47	3.85E-02	0.95	2.11E-04	0.81	7.47E-03	0.42

Table 6: FEM-MsFEM error at $\frac{\epsilon}{h} = 0.32$, $N = 32$.

h	ϵ	$\ e_{u_p}\ _{L^2}$	Order	$\ e_{u_f}\ _{H^1}$	Order	$\ e_{\phi_p}\ _{L^2}$	Order	$\ e_{\phi_p}\ _{H^1}$	Order
1/16	0.02	4.79E-03		5.07E-01		1.16E-04		8.05E-03	
1/32	0.01	1.27E-03	1.92	2.69E-01	0.92	9.57E-05	0.28	5.76E-03	0.48
1/64	0.005	3.33E-04	1.92	1.41E-01	0.93	9.42E-05	0.02	5.13E-03	0.17
1/128	0.0025	8.87E-05	1.91	7.41E-02	0.93	9.07E-05	0.06	4.90E-03	0.07

References

- [1] Assyr Abdulle and Ondrej Budáč. An adaptive finite element heterogeneous multiscale method for stokes flow in porous media. *Multiscale Modeling & Simulation*, 13(1):256–290, 2015.
- [2] Ilona Ambartsumyan, Eldar Khattatov, ChangQing Wang, and Ivan Yotov. Stochastic multiscale flux basis for stokes-darcy flows. *Journal of Computational Physics*, 401:109011, 2020.
- [3] Rodolfo Araya, Christopher Harder, Diego Paredes, and Frédéric Valentin. Multiscale hybrid-mixed method. *SIAM Journal on Numerical Analysis*, 51(6):3505–3531, 2013.
- [4] Todd Arbogast, Gergina Pencheva, Mary F. Wheeler, and Ivan Yotov. A multiscale mortar mixed finite element method. *Multiscale Modeling & Simulation*, 6(1):319–346 (electronic), 2007.
- [5] Gordon S Beavers and Daniel D Joseph. Boundary conditions at a naturally permeable wall. *Journal of fluid mechanics*, 30(1):197–207, 1967.
- [6] Susanne C Brenner. *The mathematical theory of finite element methods*. Springer, 2008.
- [7] Zhiming Chen and Thomas Y. Hou. A mixed multiscale finite element method for elliptic problems with oscillating coefficients. *Mathematics of Computation*, 72(242):541–576, 2003.
- [8] Eric T. Chung, Yalchin Efendiev, and Chak Shing Lee. Mixed generalized multiscale finite element methods and applications. *Multiscale Modeling & Simulation*, 13(1):338–366, 2015.
- [9] Marco Discacciati, Edie Miglio, and Alfio Quarteroni. Mathematical and numerical models for coupling surface and groundwater flows. *Applied Numerical Mathematics*, 43(1-2):57–74, 2002.
- [10] Y. Efendiev, V. Ginting, T. Hou, and R. Ewing. Accurate multiscale finite element methods for two-phase flow simulations. *Journal of Computational Physics*, 220(1):155–174, 2006.
- [11] Yalchin Efendiev, Juan Galvis, and Thomas Y. Hou. Generalized multiscale finite element methods (GMsFEM). *Journal of Computational Physics*, 251:116–135, 2013.
- [12] Vivette Girault, Danail Vassilev, and Ivan Yotov. Mortar multiscale finite element methods for stokes–darcy flows. *Numerische Mathematik*, 127(1):93–165, 2014.
- [13] Hadi Hajibeygi and Patrick Jenny. Multiscale finite-volume method for parabolic problems arising from compressible multiphase flow in porous media. *Journal of Computational Physics*, 228(14):5129–5147, 2009.
- [14] Thomas Y. Hou and Xiao-Hui Wu. A multiscale finite element method for elliptic problems in composite materials and porous media. *Journal of computational physics*, 134(1):169–189, 1997.
- [15] Yanren Hou and Yi Qin. On the solution of coupled stokes/darcy model with beavers–joseph interface condition. *Computers & Mathematics with Applications*, 77(1):50–65, 2019.
- [16] T. Hughes, G. Feijoo, L. Mazzei, and J. Quincy. The variational multiscale method - a paradigm for computational mechanics. *Computer Methods in Applied Mechanics and Engineering*, 166:3–24, 1998.
- [17] Patrick Jenny, SH Lee, and Hamdi A Tchelepi. Multi-scale finite-volume method for elliptic problems in subsurface flow simulation. *Journal of computational physics*, 187(1):47–67, 2003.
- [18] William J Layton, Friedhelm Schieweck, and Ivan Yotov. Coupling fluid flow with porous media flow. *SIAM Journal on Numerical Analysis*, 40(6):2195–2218, 2002.
- [19] Axel Målqvist and Daniel Peterseim. Localization of elliptic multiscale problems. *Mathematics of Computation*, 83(290):2583–2603, 2014.

- [20] E Weinan, Bjorn Engquist, Xiantao Li, Weiqing Ren, and Eric Vanden-Eijnden. Heterogeneous multiscale method: A review. *Communications in Computational Physics*, 2:367–450, 2007.
- [21] Ulrich Wilbrandt. *Stokes–Darcy Equations: Analytic and Numerical Analysis*. Springer, 2019.
- [22] Changqing Ye, Hao Dong, and Junzhi Cui. Convergence rate of multiscale finite element method for various boundary problems. *Journal of Computational and Applied Mathematics*, 374:112754, 2020.
- [23] Na Zhang, Jun Yao, Zhaoqin Huang, and Yueying Wang. Accurate multiscale finite element method for numerical simulation of two-phase flow in fractured media using discrete-fracture model. *Journal of Computational Physics*, 242:420–438, 2013.
- [24] Na Zhang, Jun Yao, Shifeng Xue, and Zhaoqin Huang. Multiscale mixed finite element, discrete fracture–vug model for fluid flow in fractured vuggy porous media. *International Journal of Heat and Mass Transfer*, 96:396–405, 2016.